Study of hybrid organic–inorganic halide perovskite solar cells based on MAI[(PbI2)1–x(CuI)x] absorber layers and their long-term stability

Wissal Belayachi, Salma Boujmiraz, Salma Zouhair, Kübra Yaşaroğlu, Guy Schmerber, Jean-Luc Rehspringer, Thomas Fix, Abdelilah Slaoui, Mohammed Abd-Lefdil, Aziz Dinia

Study of hybrid organic-inorganic halide perovskite solar cells based on MAI[$(PbI_2)_{1-x}(CuI)_x$] absorber layers and their long-term stability.

Wissal Belayachi [1, 2 *], Salma Boujmiraz [3], Salma Zouhair [3, **], Kübra Yaşaroğlu [1, 4], Guy Schmerber [1], Jean-Luc Rehspringer [1], Thomas Fix [5], Abdelilah Slaoui [5], Mohammed Abd-Lefdil [2] and Aziz Dinia [1].

[1] Université de Strasbourg, CNRS, Institut de Physique et Chimie des Matériaux de Strasbourg, UMR 7504, 23 rue du Loess, F-67000 Strasbourg, France.

[2] Université Mohammed V de Rabat, Faculté des Sciences, MANAPSE, B.P. 1014, 10000 Rabat, Morocco.

[3] Al Akhawayn University, Avenue Hassan II, 53000 Ifrane, Morocco.

[4] Fraunhofer-Institute for Solar Energy Systems ISE, Heidenhofstraße 2, 79110 Freiburg, Germany.

[5] Université de Strasbourg, CNRS, Laboratoire Icube, UMR 7357, F-67000 Strasbourg, France.

***** Correspondence: wissal.belayachi@ipcms.unistra.fr.

****** Current affiliation at the time of publication:

a. Fraunhofer Institute for Solar Energy Systems ISE, Heidenhofstr. 2, 79110 Freiburg, Germany.

b. University Abdelmalek Essaadi, Faculty of Sciences and Techniques (FST), 90000 Tangier, Morocco.

Abstract:

One of the major perovskites used as a light absorber in perovskite solar cells (PSCs) is methylammonium lead iodide (MAPI). MAPI perovskite shows many optimal optoelectronic properties making it a high-performance solar cell material. Nonetheless, PSCs face some limitations related to stability and degradation against moisture, and toxicity due their lead content. The goal of this work is to study the partial substitution of lead iodide (PbI_2) with the inorganic compound copper iodide (CuI) to enhance the solar cell stability thanks to the hydrophobic properties of the latter. XRD showed a tetragonal crystal structure growth for the MAI[$(PbI_2)_{1-x}(CuI)_x$] perovskite films. Even for 20 mol%, CuI was well incorporated into the perovskite lattice structure producing a slight change in the lattice parameters. SEM analysis showed a clear improvement of the film's morphology with the CuI substitution (less pinholes, better uniformity). The optical absorption edges and calculated optical bandgap, around 1.55 eV, remain unchanged with CuI partial substitution. With the increase in CuI/PbI_2 ratio photovoltaic properties of the MAI[$(PbI_2)_{1-x}(CuI)_x$] devices improved, higher V_{OC} and J_{SC} are observed. Finally, the stability was studied during 150 days in air and an enhancement of PSCs properties was observed for CuI substituted PbI_2 PSCs.

Keywords: Perovskite solar cell; methylammonium lead iodide ($MAPbI_3$); substitution; lead iodide (PbI_2); copper iodide (CuI); long-term stability.

Declarations:

- **Funding:** This research was co-funded by H2020-MSCA-RISE-777968 and the Erasmus+ Program of the European Union, grant number 573722.
- **Acknowledgments:** The authors thank the SEM platform of CNRS-Cronenbourg, especially Cedric Leuvrey for the SEM and EDX observations, the DRX platform (IPCMS, Strasbourg), especially Marc Lenertz for the DRX observation and Nicolas Zimmerman (Icube, Strasbourg) for the deposition of the gold contacts. W.B. thanks the H2020 Marie Skłodowska-Curie Actions program and the Erasmus+ Program of the European Union project for financial support.
- **Conflicts of Interest:** The authors declare no conflict of interest. The funders had no role in the design of the study; in the collection, analyses, or interpretation of data; in the writing of the manuscript, or in the decision to publish the results.
- **Availability of data and material:** The authors confirm that the data supporting the findings of this study are available within the article. All data and materials comply with field standards.
- **Code availability**: Not applicable.
- **Author Contributions:** Conceptualization, Jean-Luc Rehspringer and Aziz Dinia; Formal analysis, Wissal Belayachi; Funding acquisition, Abdelilah Slaoui, Mohammed Abd-Lefdil and Aziz Dinia; Investigation, Wissal Belayachi, Salma Boujmiraz, Salma Zouhair, Kübra Yaşaroğlu and Cédric Leuvrey; Methodology, Kübra Yaşaroğlu, Guy Schmerber, Cédric Leuvrey, Jean-Luc Rehspringer, Thomas Fix and Nicolas Zimmermann; Project administration, Abdelilah Slaoui, Mohammed Abd-Lefdil and Aziz Dinia; Resources, Guy Schmerber, Thomas Fix, Abdelilah Slaoui, Mohammed Abd-Lefdil and Aziz Dinia; Supervision, Kübra Yaşaroğlu, Guy Schmerber, Abdelilah Slaoui, Mohammed Abd-Lefdil and Aziz Dinia; Validation, Jean-Luc Rehspringer, Mohammed Abd-Lefdil and Aziz Dinia; Visualization, Wissal Belayachi; Writing – original draft, Wissal Belayachi; Writing – review & editing, Wissal Belayachi, Kübra Yaşaroğlu, Guy Schmerber, Jean-Luc Rehspringer, Thomas Fix, Abdelilah Slaoui, Mohammed Abd-Lefdil and Aziz Dinia.
- **Ethics approval:** Not applicable.
- **Consent to participate:** Not applicable.
- **Consent to for publication:** Not applicable.

Relevance Summary:

The work presented distinguishes itself from past work by its approach. The substitution of the lead component with the inorganic copper iodide was never studied as a mean to improve the stability of the perovskite solar cells. The results presented in this paper show the long-term stability of the perovskite solar cells elaborated and stored in ambient air. The approach and results presented represent this paper's contribution to the advancement of the state-of-the-art.

1. Introduction

Organo-lead halide-based perovskite solar cells (PSCs) have long attracted the attention of the scientific community due to the rapid growth of their achievable power conversion efficiency (PCE) [1, 2]. Since the initial report of 3.8% [3], the highest certified PCE of 25.2% [4] was achieved in a decade, making PSCs the fastest advancing solar cell technology to date. PSCs present many advantages such as low-cost and low-temperature fabrication possibilities, available and easily processable raw materials, high open-circuit voltage, bandgap tunability, and large diffusion length of charge carriers [5–7]. The structure of perovskite materials is similar to the mineral calcium titanium oxide, with ABX_3 as chemical formula, where A is an organic, non-organic or hybrid cation, B a metal ion, and X a halide [8]. Among the perovskites used, methylammonium lead halide perovskite ($CH_3NH_3PbX_3$,; CH_3NH_3 = MA) and its mixed-halide crystals are the most employed and thus have been studied in depth [9–15].

The perovskite films can be elaborated through various deposition techniques [16], from solution-based deposition techniques [17–19] to vapor assisted techniques [20–24]. As for the PSCs devices configuration, multiple device's architectures have been developed such as the mesoporous structure [11, 25, 26], the mesoporous superstructure [12, 27], the planar structure [20, 25], the inverted planar structure [25, 28, 29] and most recently the multijunction configuration [30–32].

However, a major obstacle to the industrialization of the PSCs is the low long-term stability of the devices [33–35]. PSCs are known to degrade by both extrinsic (relative humidity [36–38], temperature [37, 39], oxygen [40] and UV-light [41, 42]) and intrinsic parameters (thermal and electric field induced degradation [43–45], interfacial reactions due to defects or imperfections at grain boundaries [46, 47], corrosion of the contacts by inherent ionic defects in bulk perovskite [34, 44, 45]).

To avoid these problems and to improve the perovskite material as well as the based PV solar cells performances, various tracks have been explored such as mixed halide perovskites [48, 49], mixed-cation [50–52], mixed halide and mixed cation [53], chemical inhibition and passivation [54–57], additives [58–62], the introduction of a buffer or water proof layers [63–65], replacing organic electron/hole transport layers with inorganic materials [66–69].

Another important issue is the toxicity of lead [70], which led researchers to study the metal substitution of the lead compound [71–75]. Most of these reports mention the effects on the characteristics of the devices but not the effects on the long-term stability of the perovskite materials. Among the possible metals, copper has been studied for partial substitution of lead [74, 76] and these studies showed a slight improvement or no improvement at all in the photovoltaic properties of the devices, but none mention the results on the stability of the PSCs. On the other hand, A. Christians et al used copper iodide (CuI) as an inorganic hole conductor material for the organo-lead halide perovskite [66] and the resulting PSCs exhibited stability at high humidity when stored without encapsulation under ambient conditions.

In this paper, our overall goal is to try to improve stability while reducing the toxicity of the materials. We therefore partially substitute lead iodide (PbI_2) with the hydrophobic copper iodide (CuI), in the classical methylammonium lead iodide (MAPI or $MAPbI_3$) perovskite. The structural and optical properties of the obtained $MAI[(PbI_2)_{1-x}(CuI)_x]$ perovskite thin films were investigated as well as the photovoltaic properties of $MAI[(PbI_2)_{1-x}(CuI)_x]$ based solar cells. The long-term stability of these PSCs under ambient conditions, without use of encapsulation, was also studied.

2. Materials and Methods

2.1. Materials

Lead iodide (PbI_2, 99.999%), copper(I) iodide (CuI, ≥99.995%), anhydrous dimethylformamide (DMF) ($HCON(CH_3)_2$, 99.8%), 4-tert-butyl pyridine (4-tBp) ($C_9H_{13}N$, 96%), Spiro-MeOTAD ($C_{81}H_{68}N_4O_8$, 99%), anhydrous chlorobenzene (C_6H_5Cl , 99.8%), and anhydrous acetonitrile (CH_3CN, 99.8%) were purchased from Sigma-Aldrich. Methylammonium iodide (MAI) (CH_5NHI, ≥98%) and Lithium Bis(trifluoromethanesulfonyl) (Li-TFSI) ($C_2F_6LiNO_4S_2$, 99.95%) were purchased from Tokyo Chemical Industry (TCI). 2-propanol (IPA) ($(CH_3)_2CHOH$, 99.5%) was purchased from Carlo Erba. IPA was stored in a bottle containing zeolite sieves to ensure the adsorption of any moisture excess that might be present in the solvent. All the chemicals, other than IPA, were directly used without further purification.

2.2. Perovskite and solar cell fabrication

2.2.1. Perovskite thin films preparation

A two-step sequential spin-coating procedure was applied for the synthesis of the perovskite films. The lead precursor solution (c = 1 mol×L^{-1}) was prepared by dissolving PbI_2 and CuI, with a molar ratio of x:1−x (x being the CuI molar ratio, ranging between 0 and 0.2), in DMF. Then, the solution was heated and stirred on a hot plate at 70°C for 30 min. For the preparation of the methylammonium precursor solution (c = 0.25 mol×L^{-1}), MAI was dissolved in IPA with the desired molar ratio.

In order to characterize the active layer, $MAI[(PbI_2)_{1-x}(CuI)_x]$ thin films deposited on glass substrates were prepared. First, the lead-copper precursor solutions were spin coated on the glass substrates (2 cm × 2 cm) at 2000 rpm for 30s, followed by a first annealing at 70 °C for 3 min and a second one at 90 °C for 5 min. In the second step, the methylammonium solution was dropwise deposited on previous film, after a 30s reaction time the excess was removed by spin-coating at 2000 rpm for 30s. The resulting films are then annealed at 90 °C for 30 min in air.

2.2.2. Hole transporting layer solution preparation

First, a lithium solution was prepared by dissolving 0.023 g of Li-TFSI in 45 µL of acetonitrile. Then, 9 µL of the lithium solution, 19.5 µL of 4-tBp and 0.5 mL of chlorobenzene were added to 0.036 g of Spiro-MeOTAD.

2.2.3. Device fabrication

Fluorine-doped tin oxide (FTO) coated glass substrates (2 cm × 2 cm), coated with a TiO_2 blocking layer and a scaffolding layer, were purchased from Solaronix company (Switzerland). The substrates were cleaned by sequential ultra-sonication baths in acetone, ethanol, and deionized water for 5 min each. The cleaned substrates were then dried under N_2 gas flow and treated in a plasma cleaner with oxygen plasma for 3 min to remove the last residual organics. Yellow polyimide tape has been accurately applied to both edges of the front side to ensure that there is no deposition of $MAI[(PbI_2)_{1-x}(CuI)_x]$ on the edges that are reserved for electrical contacts. The $MAI[(PbI_2)_{1-x}(CuI)_x]$ film was deposited on top of the TiO_2 scaffolding layer by the two-step spin-coating procedure, previously detailed. The hole transporting layer was then deposited by spin

coating at 2000 rpm for 30s. Finally, a 90 nm-thick gold (Au) electrode was deposited by thermal evaporation, under a high vacuum (5×10^{-6} to 2×10^{-7} Torr), through a shadow mask with an active area of 0.25 cm^2.

2.3. Characterization

X-ray powder diffraction (XRD) patterns of polycrystalline material were collected using a Bruker-AXS D8 Advance X-ray diffractometer with CuKα_1 radiation (λ = 1.54056 Å) in the 2θ range of 10 – 60° with a step size of 0.02° and a time setting of 1s per step. Phase analysis was conducted using XRD software Eva.

Scanning electron microscopy (SEM) was performed using a field emission scanning electron microscope (FSEM JEOL 6700F) coupled with an Energy Dispersive X-ray (EDX) analyzer. The SEM scans were recorded for 15K and 30K magnification and at 5 kV applied voltage. The EDX analyzes were acquired at 7 kV applied voltage.

UV-Vis spectroscopy was carried out using a Perkin-Elmer Lambda 950 spectrophotometer over the spectral range 200 – 1200 nm. An integrating sphere was used to collect both, specular and diffuse transmittance to reduce the effect of light scattering originated from refraction and reflection phenomena on the perovskite crystals.

The current density-voltage (J-V) characteristics were recorded with a Keithley 2400 source meter and 300 W collimated Xenon lamp (Newport) calibrated with the light intensity to 100 $mW.cm^{-2}$ under AM 1.5 G solar light condition using a certified silicon solar cell. The optical area of the devices measured is 0.25 cm^2, and no mask was used during the measurements.

3. Results and Discussion

3.1. Structure and morphology

3.1.1. X-Ray Diffraction

The XRD pattern of the MAI[$(PbI_2)_{1-x}(CuI)_x$] films deposited on glass substrates are shown in Fig. 1a. The most intense $MAPbI_3$ perovskite characteristic peaks are located at approximately 14.12° and 28.52° (2θ), corresponding to the (110) and (220) lattice planes, respectively. These peaks are observed for our $MAPbI_3$ and MAI[$(PbI_2)_{1-x}(CuI)_x$] ($0.1 \leq x \leq 0.2$) samples. The diffraction peaks profile and values of the MAI[$(PbI_2)_{1-x}(CuI)_x$] perovskite films are in good agreement with those of the literature as well as with the tetragonal phase of the $MAPbI_3$ perovskite (JCPDS file n° 01-083-7582) [77]. No residual CuI or a Cu-based by-product is observed in the detection limit of XRD. For the (001) lattice plane of PbI_2, the characteristic peak is still present even with the increase of the CuI doping level. This leads to believe that the CH_3NH_3I reaction hardly proceeds beyond the surface of the PbI_2 (or PbI_2-CuI) films, and that the complete transformation of all the crystalline structure requires a change in the deposition process parameters. A new peak is observed at lower angles (11.54°) which might be an indicator to the presence of this complex or a MAPI-based by-product such as observed by Leguy et al [78].

The texture coefficient (T_C), which represents the texture of a particular plane, was calculated for each film (Table 1). T_C of a particular plane is defined by the well-known relation [79] (equation 1):

$$T_C(hkl) = \frac{I(hkl)/I_0(hkl)}{m^{-1}\sum_1^m I(hkl)/I_0(hkl)}, \quad (1)$$

where I(hkl) is the measured relative intensity of a plane (hkl), I_0(hkl) the standard intensity of the plane (hkl) taken from JCPDS data and m the number of diffraction peaks. The deviation from unity of T_C implies the preferred growth direction.

Table 1 Texture coefficient of the MAI[$(PbI_2)_{1-x}(CuI)_x$] films.

hkl	T_C [MAPI]	T_C [MAPI : 10% CuI]	T_C [MAPI : 20% CuI]
002	0	0	1.8
110	3.1	1.8	1.6
004	0	0.14	3.0
220	3.3	1.5	0.68

For the classic MAPI film, the preferred growth direction is the direction of the (110) plane (Table 1). The same growth direction is found for the MAPI : 10% CuI film. Additionally, the texture coefficient relative to the (002) and (004) lattice planes increased, sign of the emergence of the peaks characteristic of the (002) and (004) lattice planes. Lastly, for MAPI : 20% CuI the growth direction changed over to the direction of the (002) plane, the film's growth direction is now perpendicular to the substrate's surface rather than diagonal.

The crystallite size of MAI[$(PbI_2)_{1-x}(CuI)_x$] films is estimated using the Scherrer formula [80] (equation 2):

$$D = \frac{K\lambda}{\beta\cos(\theta)}, \quad (2)$$

where D is the average crystallite size perpendicular to the reflecting planes, λ is the X-ray light wavelength, β is the width of the X-ray peak on the 2θ axis, normally measured as full width at half maximum (FWHM), θ is the Bragg angle, and K is the so-called Scherrer constant. K depends on the crystallite shape and the size distribution, indices of the diffraction line, and the actual definition used for β whether FWHM or integral breadth [81]. K can have values anywhere from 0.62 and 2.08. In this paper, K = 0.94 was used. In this work, the calculated values of D represent estimates (discussion on the accuracy of Equation (2) can be found in the literature [82]).

The reported values are an average of the crystallite size determined for the peaks characteristic of the (002), (110), (004) and (220) lattice planes. The crystallite size increases with the introduction of CuI in the lead precursor solution (Table 2).

Table 2 Estimated cell parameters and crystallite size of the MAI[$(PbI_2)_{1-x}(CuI)_x$] films.

Sample	a=b (Å)	c (Å)	Unit cell volume (Å^3)	Crystallite Size (nm)
MAPI	8.862 ± 0.004	12.655 ± 0.011	993.8 ± 1.6	79 ± 4
MAPI : 10% CuI	8.841 ± 0.010	12.628 ± 0.014	987.1 ± 3.4	101 ± 8
MAPI : 20% CuI	8.841 ± 0.010	12.633 ± 0.010	987.6 ± 2.9	135 ± 5

To determine the lattice parameters, a refinement of the XRD patterns was carried out using FullProof software, the results are presented in Table 2. It is observed that increasing the CuI doping ratio led to a decrease of the lattice parameter a (respectively the lattice parameter b) and the lattice parameter c. Previous studies demonstrated that the incorporation of ions with smaller ionic radius in $MAPbI_3$ could reduce the lattice constant [71, 83] thus the change in the lattice parameters is a result of the Pb^{2+} ions (119 pm) being partially replaced by the smaller sized Cu^{+} ions (73 pm) [72] at the B-sites of the perovskite lattice. However, the absence of change of the lattice parameter a and c between the films containing 10% and 20% of CuI in molar ratio leads to believe that no further substitution of the Pb^{2+} ions is taking place.

These results demonstrate that the structure was sensitively affected by the insertion of metal cation in the perovskite structure. When the CuI content is above 10%, the substitution of PbI_2 with CuI results in no changes to the structure.

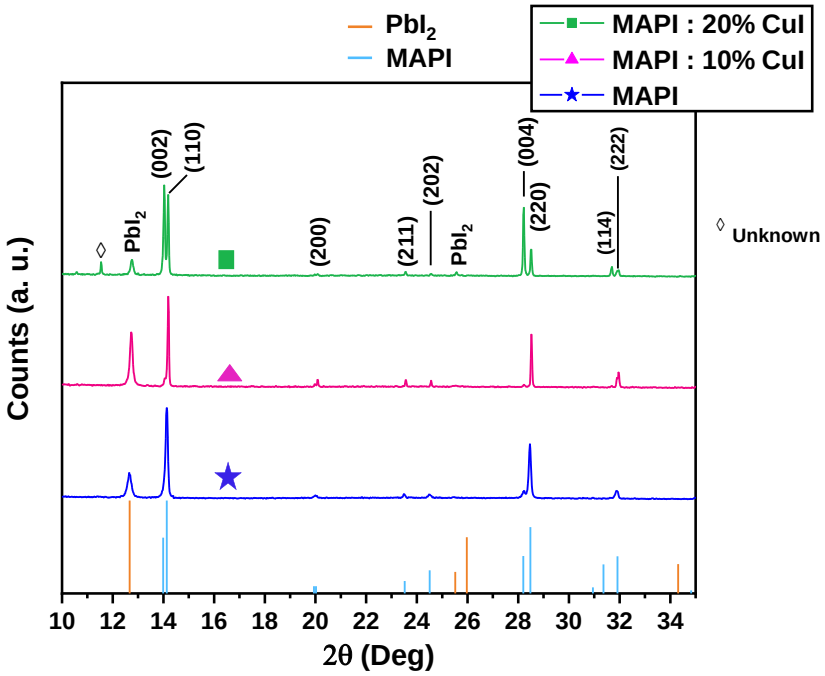

(**a**)

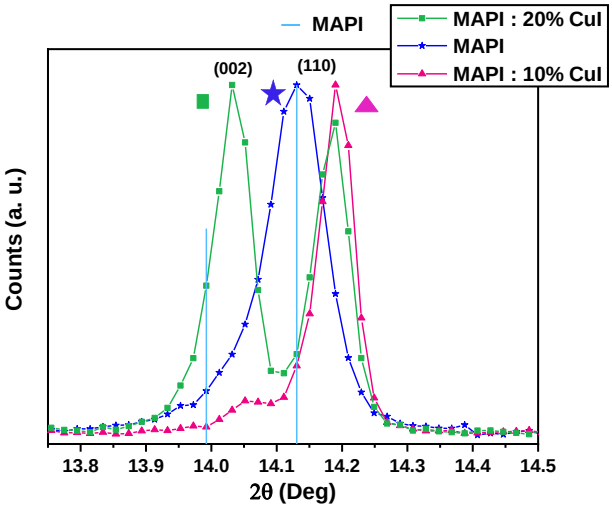

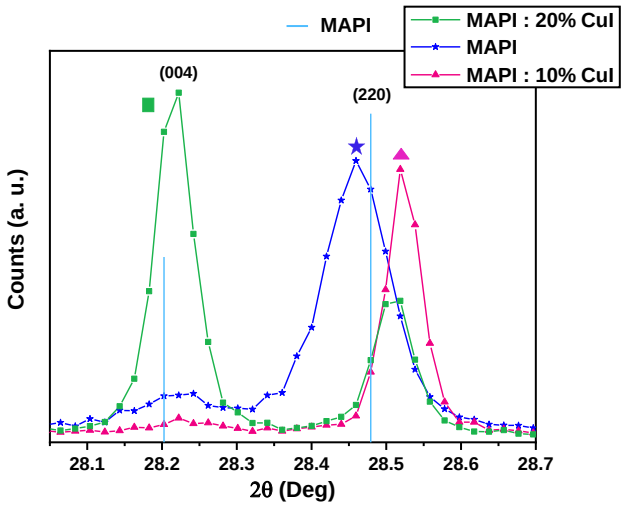

(**b**) (**c**)

Fig. 1 (**a**) X-ray diffraction pattern of MAI[$(PbI_2)_{1-x}(CuI)_x$] films deposited on glass substrates with different CuI incorporation concentrations, (**b**) a zoom-in of the XRD pattern at (110) lattice plane and (**c**) a zoom-in of the XRD pattern at (220) lattice plane.

3.1.2. SEM characterization

Scanning electronic microscope (SEM) analysis was conducted to investigate the impact of the partial PbI_2 substitution with CuI on the surface morphology. The surface SEM images of the MAI[$(PbI_2)_{1-x}(CuI)_x$] films deposited on glass substrates are presented in Fig. 2. The pure $MAPbI_3$ film (Fig. 2a) is composed of densely packed needle-like grains with the domain size distributing in a range of 0.4 - 2 µm, which are composed of smaller crystals based on the crystallite sizes in Table 1. With the addition of CuI, the morphology of the perovskite is improved (Fig. 2b and 2c). The films surface appears to be more homogeneous. The films show more regular shaped grains and a decrease in pinholes density. The grain size also increases with the increase of the CuI/PbI_2 ratio. The grain growth reduces the relative number of pinholes and induces a better surface coverage. Surface between the grains exposed to moisture is reduced which would contribute to improving the long-term stability. Notice that these observations are in good agreement with XRD texture coefficient. Moreover, the perpendicular growth of CuI doped samples could be a less moisture sensitive crystalline orientation.

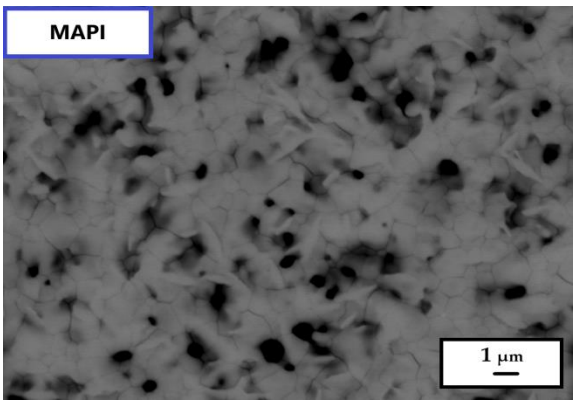

(**a**)

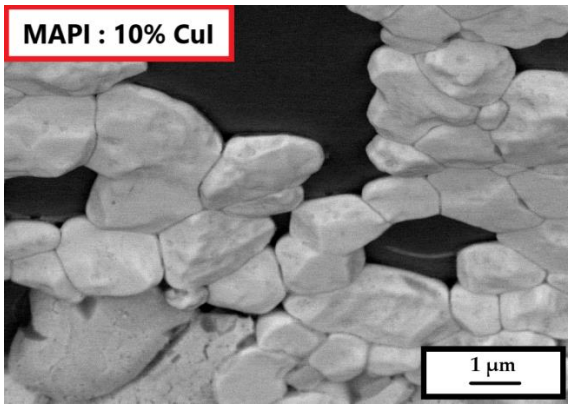

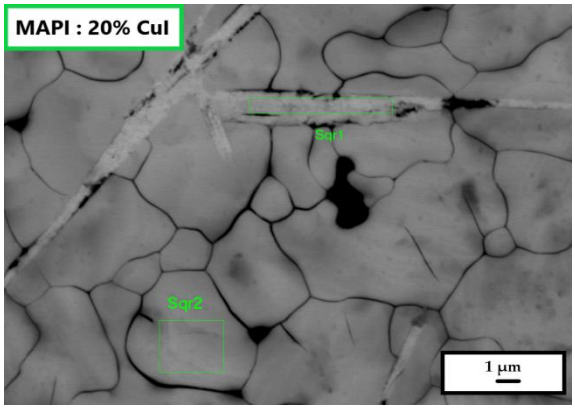

(**b**) (**c**)

Fig. 2 (**a-c**) Surface SEM images of the MAI[$(PbI_2)_{1-x}(CuI)_x$] films deposited on glass substrates.

3.2. Optical properties

The absorption spectrum of MAI[$(PbI_2)_{1-x}(CuI)_x$] films deposited on glass substrate are displayed in inset of Fig. 3. The absorption edges span from 740 up to 780 nm.

The incident photon energy (hυ) and E_g are related through Tauc's equation [84]:

$$(\alpha h\upsilon) = \beta\left(h\upsilon - E_g\right)^{\frac{1}{n}}, \tag{3}$$

where α is the absorption coefficient, E_g the optical bandgap energy, β the constant depending on (hυ) and n is related to the type of band transition (2 or 1/2 for direct and indirect transitions, respectively). The absorption coefficient α is calculated through the following relation:

$$\alpha = \frac{1}{d}\ln\left(\frac{1}{T}\right), \tag{4}$$

where T is the optical transmission and d the thickness of the sample. d is estimated to be around 330 nm (determined by profilometric analysis).

In the assumption of a direct band transition for the tetragonal $MAPbI_3$ perovskite [26, 85], the optical bandgap (E_g) of the samples was estimated by extrapolating the linear part of Tauc's plots ($(\alpha h\nu)^2$ vs. (hν)) that intercepts the energy axis (Fig. 3). The estimated bandgap of MAI[$(PbI_2)_{1-x}(CuI)_x$] are 1.56 ± 0.05 eV for $MAPbI_3$, 1.55 ± 0.05 eV for MAPI : 10% CuI and 1.58 ± 0.05 eV for MAPI : 20% CuI. The estimated E_g are in agreement with the reported value for tetragonal $MAPbI_3$ perovskite (1.55 eV) [10, 85] and are barely affected by the change in CuI fraction. It also remains close to the optimal band gap for photovoltaic performance (1.4 eV).

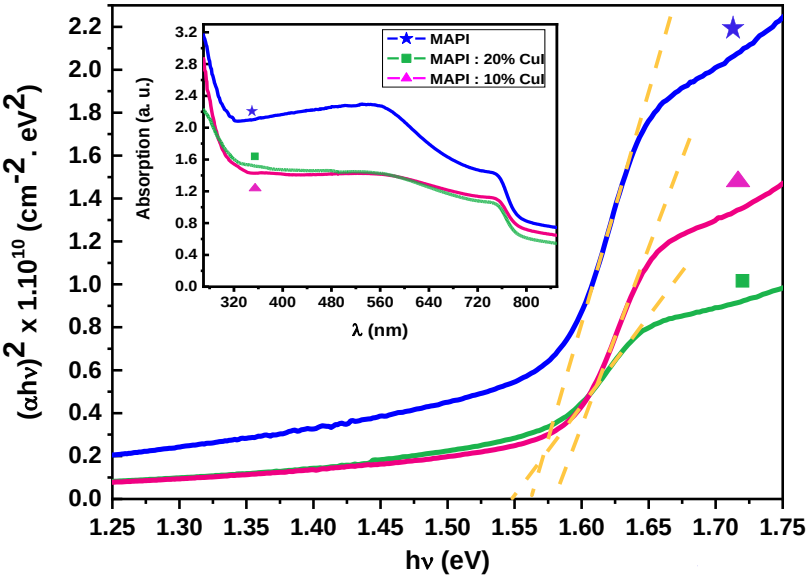

Fig. 3. UV - Visible absorption spectra of the MAI[$(PbI_2)_{1-x}(CuI)_x$] films and Tauc's plots show a slight variation in optical bandgap of the MAI[$(PbI_2)_{1-x}(CuI)_x$] films.

3.3. Photovoltaic devices

3.3.1. Performance

The current density–voltage (J–V) characteristics for the MAI[$(PbI_2)_{1-x}(CuI)_x$] based photovoltaic devices are shown in Fig. 4, and the photovoltaic characteristics are listed in Table 3. Overall, the various devices presented low photovoltaic performance compared to the literature.

For the $MAPbI_3$ device, the very low photovoltaic performances are attributed to the existence of pinholes, as observed in Fig. 2. The pinholes compromise the efficiency by introducing shunt paths in the device. When Pb^{2+} is substituted with Cu^+, the photovoltaic characteristics are slightly improved, except for the short circuit current density (J_{SC}) and series resistance (R_S). Indeed, for the MAPI : 20% device the fill factor (FF) increases from 23.4 up to 69.1 %, and the open circuit voltage (V_{OC}) from 120.1 up to 869 mV. Consequently, a slight enhancement of power conversion efficiency (PCE) is observed. Furthermore, the MAPI : 20% device exhibits the largest shunt resistance (R_{Sh}), an indicator of the lessening of shunt paths in the device (reduction of pinholes), as witnessed by the higher FF and V_{OC}. The results are promising and show an effect of the partial substitution of PbI_2 by CuI, which was not the case in the work reported by Frolova et al. They found that there is no benefit to the substitution of Pb^{2+} with monovalent ions, such as Cu^+ or Ag^+ [74].

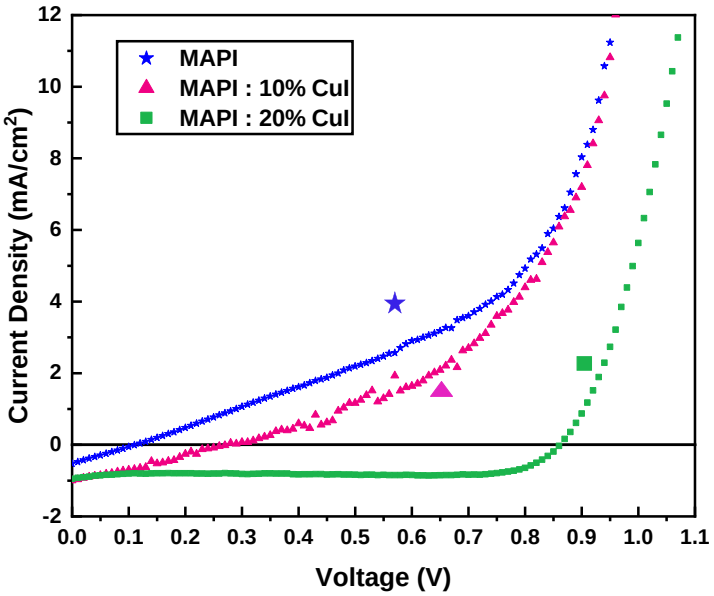

Fig. 4 Photocurrent-Voltage (J-V) characteristics of the MAI[$(PbI_2)_{1-x}(CuI)_x$] based photovoltaic devices.

Table 3 Photovoltaic characteristics of the MAI[$(PbI_2)_{1-x}(CuI)_x$] based photovoltaic devices

	MAPI	**MAPI : 10% CuI**	**MAPI : 20% CuI**
J_{sc} (mA/cm^2)	0.53	1.0	0.95

V_{oc} (mV)	120	275	864
FF (%)	23.4	29.5	69.1
PCE (%)	0.02	0.08	0.57
R_{Sh} ($\Omega.cm^2$)	178 ± 4	196 ± 12	8736 ± 559
R_S ($\Omega.cm^2$)	11.9 ± 0.1	15.6 ± 0.2	44 ± 2

3.3.3. SEM and EDX analysis

The cross-sectional SEM images of the complete MAI[$(PbI_2)_{1-x}(CuI)_x$] based photovoltaic devices with glass/ FTO/TiO_2 compact layer/ mesoporous TiO_2/perovskite/ spiro-OMeTAD/Au are shown in Fig. 5. One can clearly see that the partial substitution of PbI_2 with CuI has a strong impact on the structure of the solar cells. Indeed, a better pore-filling within the mesoporous TiO_2 scaffold is observed with the increase of CuI/PbI_2 ratio. This improvement in pore filling induces an expansion of the contact area between the perovskite and TiO_2 improving therefore carrier exchange and transport. Additionally, the thickness of the layer of non-infiltrated perovskite, or overlayer, decreases with the increase of CuI content. The thickness of the overlayer went from approximatively 200 nm for the $MAPbI_3$ device to 145 nm for the MAPI : 10% CuI device and 115 nm for the MAPI : 20% CuI device. The spiro-OMeTAD layer and gold contact are also better deposited with the increase of CuI/PbI_2 ratio. The increased FF and V_{OC} for the MAPI : 20% CuI maybe due to the better pore-filling within the mesoporous TiO_2 scaffold compared to the imperfect pore-filling for the $MAPbI_3$ device. It must be kept in mind that TiO_2 mesoporous layer has been heat sintered at 500°C and this leads to a bad wettability by DMF. Addition of CuI seems to contribute to a better compatibility between the lead precursor solutions and TiO_2 surface. EDX analysis was carried out on the MAI[$(PbI_2)_{1-x}(CuI)_x$] based photovoltaic devices and it showed that the intensity of the peaks corresponding to the elements constituting the MAI[$(PbI_2)_{1-x}(CuI)_x$] perovskite increases with the increase of CuI fraction, which is proof of the better pore-filling within the mesoporous TiO_2 scaffold with the increase of CuI fraction. Nonetheless, the low J_{SC} suggests still an insufficient contact area within the mesoporous TiO_2 scaffold. Notice that the preparation technique, the two-step process, could be an objective reason for those low efficiencies. As on glass surface the penetration of MAI is certainly weak and a PbI_2 grabbed layer remains impinging the carrier collection.

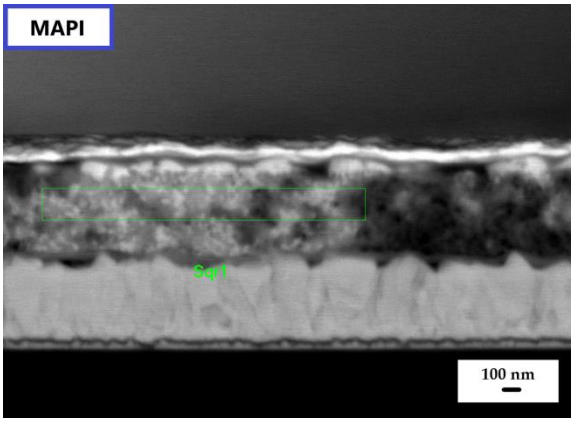

(**a**)

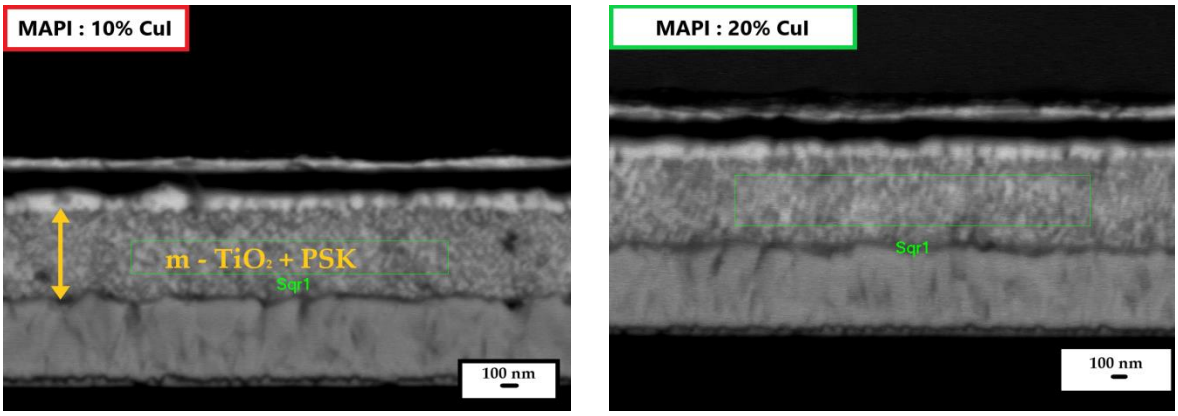

(**b**) (**c**)

Fig. 5 (**a-c**) Cross-sectional SEM images of complete MAI[$(PbI_2)_{1-x}(CuI)_x$] based photovoltaic devices.

3.3.3. Long-term stability

The evolution of the (J-V) characteristic, the J_{SC} and the PCE of the MAPI: 10% CuI based photovoltaic device as a function of time are displayed in Fig. 6, and the evolution of R_{Sh} and R_S are reported in Fig. 7. The device was stored in dark at room temperature without encapsulation. The solar cell was characterized for over four months. As previously reported, the $MAPbI_3$ perovskite solar cells are unstable in ambient air [26–28]. In our case, the initial PCE improved with time (Fig. 6b). The appearance of the (J-V) characteristic and the evolution (following an exponential) of the PCE indicate that both the PCE and stability of the device in ambient air are improved after the substitution of Pb^{2+} with Cu^{+}. The decrease of the R_S ($8x10^{-3}$ ± $2x10^{-4}$ Ω.cm^2 for day 132) is consistent with the increase of the J_{SC} (Fig. 7). However, the decrease of R_{Sh} is detrimental to any further improvement of the FF or V_{OC}. Furthermore, no change in color in the perovskite film was observed until the beginning of the fifth month. The MAPI : 10% CuI based photovoltaic device started to deteriorate due to the degradation of the perovskite layer (yellowing of the layer).

One explanation of the favorable evolution could be found in the evolution of transversal composition. It seems like a latent kinetic reaction, which improves the contact areas between the perovskite layer and the other layers, takes place over time. As detected in the layers deposited on glass substrate, after ending the two-step process a PbI_2 grabbed layer is observed. In solar cells prepared with the same two-step process we assigned the poor J_{SC} to a grabbed PbI_2 layer that limits the carrier collection. Due to mobility of methylammonium a homogenization of the present phases can occur along the time and the amount of photosensitive phase in contact with p and n layer increases leading to an improvement of cell performance and long-term stability.

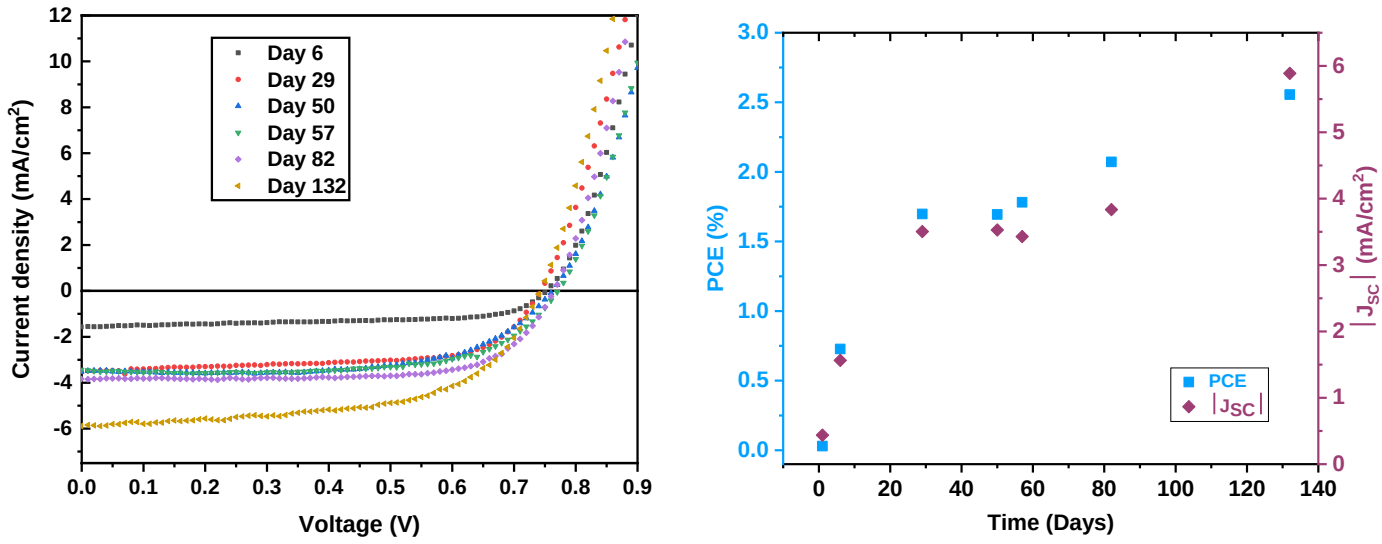

(**a**) (**b**)

Fig. 6 Evolution of (**a**) the (J-V) characteristic and (**b**) the JSC and the PCE of the MAPI : 10% CuI based photovoltaic device as a function of time after storage in dark in ambient environment at room temperature without encapsulation.

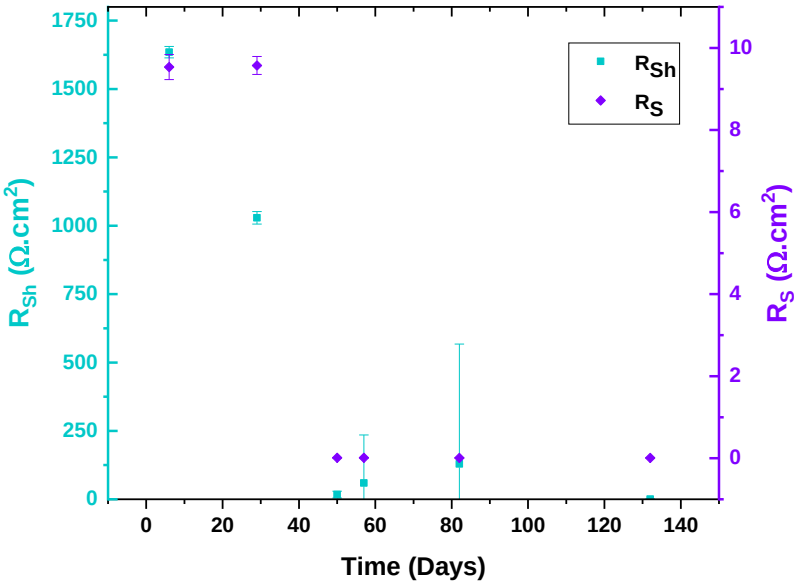

Fig. 7 : Evolution of the resistances of the MAPI : 10% CuI based photovoltaic devices as a function of time after storage in dark in ambient environment at room temperature without encapsulation.

4. Conclusions

In summary, we have studied the partial substitution of PbI_2 with CuI into the solution-processed $MAI[(PbI_2)_{1-x}(CuI)_x]$ perovskite films. XRD analysis showed that the diffraction pattern of the $MAI[(PbI_2)_{1-x}(CuI)_x]$ perovskite thin films fit with the tetragonal $MAPbI_3$ perovskite structure but residual PbI_2 was detected. Up to 10% doping ratio no impurity or by-products of CuI were observed which seems to indicate the optimum ratio for Cu incorporation in the $MAPbI_3$ lattice is 10%. SEM analysis images of the

$MAI[(PbI_2)_{1-x}(CuI)_x]$ perovskite thin films showed that the film homogeneity was improved, and the grain size was enhanced with the increase of CuI/PbI_2 ratio. The estimated optical band gaps were in agreement with the reported value for tetragonal $MAPbI_3$ perovskite (1.55 eV) and remains unaffected by the partial substitution of PbI_2 with CuI.

$MAI[(PbI_2)_{1-x}(CuI)_x]$ based photovoltaic devices fabricated by spin-coating method clearly demonstrates the effect of the partial substitution of PbI_2 with CuI on the photovoltaic properties. V_{OC}, FF and PCE improved with the increase of CuI/PbI_2 ratio. The improvement of these photovoltaic parameters might be due to the better pore-filling of perovskite with the addition of CuI observed through SEM analysis. However, the J_{SC} remains low for all devices. Nonetheless, the long-term stability of the $MAI[(PbI_2)_{1-x}(CuI)_x]$ based photovoltaic devices was improved with the partial substitution of PbI_2 with CuI.

References

1. Nakazaki J, Segawa H (2018) Evolution of organometal halide solar cells. Journal of Photochemistry and Photobiology C: Photochemistry Reviews 35:74–107. https://doi.org/10.1016/j.jphotochemrev.2018.02.002

2. Park N-G (2020) Research Direction toward Scalable, Stable, and High Efficiency Perovskite Solar Cells. Advanced Energy Materials 10:1903106. https://doi.org/10.1002/aenm.201903106

3. Kojima A, Teshima K, Shirai Y, Miyasaka T (2009) Organometal Halide Perovskites as Visible-Light Sensitizers for Photovoltaic Cells. J Am Chem Soc 131:6050–6051. https://doi.org/10.1021/ja809598r

4. Best Research-Cell Efficiency Chart. https://www.nrel.gov/pv/cell-efficiency.html. Accessed 28 Apr 2020

5. Xing G, Mathews N, Sun S, et al (2013) Long-Range Balanced Electron- and Hole-Transport Lengths in Organic-Inorganic CH3NH3PbI3. Science 342:344–347. https://doi.org/10.1126/science.1243167

6. Wehrenfennig C, Eperon GE, Johnston MB, et al (2014) High Charge Carrier Mobilities and Lifetimes in Organolead Trihalide Perovskites. Advanced Materials 26:1584–1589. https://doi.org/10.1002/adma.201305172

7. Stranks SD, Eperon GE, Grancini G, et al (2013) Electron-Hole Diffusion Lengths Exceeding 1 Micrometer in an Organometal Trihalide Perovskite Absorber. Science 342:341–344. https://doi.org/10.1126/science.1243982

8. Gao P, Grätzel M, Nazeeruddin MK (2014) Organohalide lead perovskites for photovoltaic applications. Energy Environ Sci 7:2448–2463. https://doi.org/10.1039/C4EE00942H

9. Jung HS, Park N-G (2015) Perovskite Solar Cells: From Materials to Devices. Small 11:10–25. https://doi.org/10.1002/smll.201402767

10. Castelli IE, García-Lastra JM, Thygesen KS, Jacobsen KW (2014) Bandgap calculations and trends of organometal halide perovskites. APL Materials 2:081514. https://doi.org/10.1063/1.4893495

11. Etgar L, Gao P, Xue Z, et al (2012) Mesoscopic CH3NH3PbI3/TiO2 Heterojunction Solar Cells. J Am Chem Soc 134:17396–17399. https://doi.org/10.1021/ja307789s

12. Lee MM, Teuscher J, Miyasaka T, et al (2012) Efficient Hybrid Solar Cells Based on Meso-Superstructured Organometal Halide Perovskites. Science 338:643–647. https://doi.org/10.1126/science.1228604

13. Atourki L, Vega E, Marí B, et al (2016) Role of the chemical substitution on the structural and luminescence properties of the mixed halide perovskite thin MAPbI3−xBrx (0≤x≤1) films. Applied Surface Science 371:112–117. https://doi.org/10.1016/j.apsusc.2016.02.207

14. Peng L, Hu Y, Xu L (2016) Theoretical and Experimental Research on the Bulk Photovoltaic Effect in Hybrid Organic–Inorganic Perovskites CH3NH3PbI2 X (X = Cl, Br, I). Science of Advanced Materials 8:2223–2230. https://doi.org/10.1166/sam.2016.3007

15. Gonzalez-Pedro V, Juarez-Perez EJ, Arsyad W-S, et al (2014) General Working Principles of CH3NH3PbX3 Perovskite Solar Cells. Nano Lett 14:888–893. https://doi.org/10.1021/nl404252e

16. Roy P, Kumar Sinha N, Tiwari S, Khare A (2020) A review on perovskite solar cells: Evolution of architecture, fabrication techniques, commercialization issues and status. Solar Energy 198:665–688. https://doi.org/10.1016/j.solener.2020.01.080

17. Burschka J, Pellet N, Moon S-J, et al (2013) Sequential deposition as a route to high-performance perovskite-sensitized solar cells. Nature 499:316–319. https://doi.org/10.1038/nature12340

18. Im J-H, Kim H-S, Park N-G (2014) Morphology-photovoltaic property correlation in perovskite solar cells: One-step versus two-step deposition of CH3NH3PbI3. APL Materials 2:081510. https://doi.org/10.1063/1.4891275

19. Jeon NJ, Noh JH, Kim YC, et al (2014) Solvent engineering for high-performance inorganic–organic hybrid perovskite solar cells. Nature Materials 13:897–903. https://doi.org/10.1038/nmat4014

20. Liu M, Johnston MB, Snaith HJ (2013) Efficient planar heterojunction perovskite solar cells by vapour deposition. Nature 501:395–398. https://doi.org/10.1038/nature12509

21. Chen Q, Zhou H, Hong Z, et al (2014) Planar Heterojunction Perovskite Solar Cells via Vapor-Assisted Solution Process. J Am Chem Soc 136:622–625. https://doi.org/10.1021/ja411509g

22. Mariano F, Listorti A, Rizzo A, et al (2017) Thermally evaporated hybrid perovskite for hetero-structured green light-emitting diodes. Appl Phys Lett 111:163301. https://doi.org/10.1063/1.5001828

23. Luo P, Liu Z, Xia W, et al (2015) Uniform, stable, and efficient planar-heterojunction perovskite solar cells by facile low-pressure chemical vapor deposition under fully open-air conditions. ACS Appl Mater Interfaces 7:2708–2714. https://doi.org/10.1021/am5077588

24. Abrusci A, Stranks SD, Docampo P, et al (2013) High-Performance Perovskite-Polymer Hybrid Solar Cells via Electronic Coupling with Fullerene Monolayers. Nano Lett 13:3124–3128. https://doi.org/10.1021/nl401044q

25. Kumari N, Patel SR, Gohel JV (2018) Current Progressand Future Prospective of Perovskite Solar Cells: A comprehensive Review. REVIEWS ON ADVANCED MATERIALS SCIENCE 53:161–186. https://doi.org/10.1515/rams-2018-0012

26. Kim H-S, Lee C-R, Im J-H, et al (2012) Lead iodide perovskite sensitized all-solid-state submicron thin film mesoscopic solar cell with efficiency exceeding 9%. Sci Rep 2:591. https://doi.org/10.1038/srep00591

27. Snaith HJ (2013) Perovskites: The Emergence of a New Era for Low-Cost, High-Efficiency Solar Cells. J Phys Chem Lett 4:3623–3630. https://doi.org/10.1021/jz4020162

28. Mesquita I, Andrade L, Mendes A (2018) Perovskite solar cells: Materials, configurations and stability. Renewable and Sustainable Energy Reviews 82:2471–2489. https://doi.org/10.1016/j.rser.2017.09.011

29. Tang J, Jiao D, Zhang L, et al (2018) High-performance inverted planar perovskite solar cells based on efficient hole-transporting layers from well-crystalline NiO nanocrystals. Solar Energy 161:100–108. https://doi.org/10.1016/j.solener.2017.12.045

30. Wali Q, Elumalai NK, Iqbal Y, et al (2018) Tandem perovskite solar cells. Renewable and Sustainable Energy Reviews 84:89–110. https://doi.org/10.1016/j.rser.2018.01.005

31. Yan LL, Han C, Shi B, et al (2019) A review on the crystalline silicon bottom cell for monolithic perovskite/silicon tandem solar cells. Materials Today Nano 7:100045. https://doi.org/10.1016/j.mtnano.2019.100045

32. Xie S, Xia R, Chen Z, et al (2020) Efficient monolithic perovskite/organic tandem solar cells and their efficiency potential. Nano Energy 78:105238. https://doi.org/10.1016/j.nanoen.2020.105238

33. Chen J, Cai X, Yang D, et al (2017) Recent progress in stabilizing hybrid perovskites for solar cell applications. Journal of Power Sources 355:98–133. https://doi.org/10.1016/j.jpowsour.2017.04.025

34. Wang D, Wright M, Elumalai NK, Uddin A (2016) Stability of perovskite solar cells. Solar Energy Materials and Solar Cells 147:255–275. https://doi.org/10.1016/j.solmat.2015.12.025

35. Asghar MI, Zhang J, Wang H, Lund PD (2017) Device stability of perovskite solar cells – A review. Renewable and Sustainable Energy Reviews 77:131–146. https://doi.org/10.1016/j.rser.2017.04.003

36. Tong C-J, Geng W, Tang Z-K, et al (2015) Uncovering the Veil of the Degradation in Perovskite CH3NH3PbI3 upon Humidity Exposure: A First-Principles Study. J Phys Chem Lett 6:3289–3295. https://doi.org/10.1021/acs.jpclett.5b01544

37. Han Y, Meyer S, Dkhissi Y, et al (2015) Degradation observations of encapsulated planar CH3NH3PbI3 perovskite solar cells at high temperatures and humidity. J Mater Chem A 3:8139–8147. https://doi.org/10.1039/C5TA00358J

38. Contreras-Bernal L, Aranda C, Valles-Pelarda M, et al (2018) Homeopathic Perovskite Solar Cells: Effect of Humidity during Fabrication on the Performance and Stability of the Device. J Phys Chem C 122:5341–5348. https://doi.org/10.1021/acs.jpcc.8b01558

39. Mesquita I, Andrade L, Mendes A (2019) Temperature Impact on Perovskite Solar Cells Under Operation. ChemSusChem 12:2186–2194. https://doi.org/10.1002/cssc.201802899

40. Sun Q, Fassl P, Becker-Koch D, et al (2017) Role of Microstructure in Oxygen Induced Photodegradation of Methylammonium Lead Triiodide Perovskite Films. Advanced Energy Materials 7:1700977. https://doi.org/10.1002/aenm.201700977

41. Zheng L, Xuan Y (2018) Suppressing the negative effect of UV light on perovskite solar cells via photon management. Solar Energy 173:1216–1224. https://doi.org/10.1016/j.solener.2018.08.053

42. Roesch R, Faber T, Hauff E von, et al (2015) Procedures and Practices for Evaluating Thin-Film Solar Cell Stability. Advanced Energy Materials 5:1501407. https://doi.org/10.1002/aenm.201501407

43. Wali Q, Iftikhar FJ, Khan ME, et al (2020) Advances in stability of perovskite solar cells. Organic Electronics 78:105590. https://doi.org/10.1016/j.orgel.2019.105590

44. Wang R, Mujahid M, Duan Y, et al (2019) A Review of Perovskites Solar Cell Stability. Advanced Functional Materials 29:1808843. https://doi.org/10.1002/adfm.201808843

45. Berhe TA, Su W-N, Chen C-H, et al (2016) Organometal halide perovskite solar cells: degradation and stability. Energy Environ Sci 9:323–356. https://doi.org/10.1039/C5EE02733K

46. Chouhan AS, Jasti NP, Avasthi S (2018) Effect of interface defect density on performance of perovskite solar cell: Correlation of simulation and experiment. Materials Letters 221:150–153. https://doi.org/10.1016/j.matlet.2018.03.095

47. Uratani H, Yamashita K (2017) Charge Carrier Trapping at Surface Defects of Perovskite Solar Cell Absorbers: A First-Principles Study. J Phys Chem Lett 8:742–746. https://doi.org/10.1021/acs.jpclett.7b00055

48. Liu D, Traverse CJ, Chen P, et al (2018) Aqueous-Containing Precursor Solutions for Efficient Perovskite Solar Cells. Advanced Science 5:1700484. https://doi.org/10.1002/advs.201700484

49. Kim IS, Cao DH, Buchholz DB, et al (2016) Liquid Water- and Heat-Resistant Hybrid Perovskite Photovoltaics via an Inverted ALD Oxide Electron Extraction Layer Design. Nano Lett 16:7786–7790. https://doi.org/10.1021/acs.nanolett.6b03989

50. Wang Q, Lin F, Chueh C-C, et al (2018) Enhancing efficiency of perovskite solar cells by reducing defects through imidazolium cation incorporation. Materials Today Energy 7:161–168. https://doi.org/10.1016/j.mtener.2017.09.007

51. Pellet N, Gao P, Gregori G, et al (2014) Mixed-Organic-Cation Perovskite Photovoltaics for Enhanced Solar-Light Harvesting. Angewandte Chemie International Edition 53:3151–3157. https://doi.org/10.1002/anie.201309361

52. Saliba M, Matsui T, Domanski K, et al (2016) Incorporation of rubidium cations into perovskite solar cells improves photovoltaic performance. Science 354:206–209. https://doi.org/10.1126/science.aah5557

53. Saliba M, Matsui T, Seo J-Y, et al (2016) Cesium-containing triple cation perovskite solar cells: improved stability, reproducibility and high efficiency. Energy Environ Sci 9:1989–1997. https://doi.org/10.1039/C5EE03874J

54. Back H, Kim G, Kim J, et al (2016) Achieving long-term stable perovskite solar cells via ion neutralization. Energy Environ Sci 9:1258–1263. https://doi.org/10.1039/C6EE00612D

55. Chen C, Zhuang X, Bi W, et al (2020) Chemical inhibition of reversible decomposition for efficient and super-stable perovskite solar cells. Nano Energy 68:104315. https://doi.org/10.1016/j.nanoen.2019.104315

56. Mahmud MA, Elumalai NK, Upama MB, et al (2018) Passivation of interstitial and vacancy mediated trap-states for efficient and stable triple-cation perovskite solar cells. Journal of Power Sources 383:59–71. https://doi.org/10.1016/j.jpowsour.2018.02.030

57. Zhang T, Guo N, Li G, et al (2016) A controllable fabrication of grain boundary PbI2 nanoplates passivated lead halide perovskites for high performance solar cells. Nano Energy 26:50–56. https://doi.org/10.1016/j.nanoen.2016.05.003

58. Yang L, Han G, Chang Y, et al (2019) Enhanced efficiency and stability of perovskite solar cells by synergistic effect of magnesium acetate introducing into CH3NH3PbI3. Materials Science in Semiconductor Processing 104:104671. https://doi.org/10.1016/j.mssp.2019.104671

59. Hsu H-L, Chang C-C, Chen C-P, et al (2015) High-performance and high-durability perovskite photovoltaic devices prepared using ethylammonium iodide as an additive. J Mater Chem A 3:9271–9277. https://doi.org/10.1039/C5TA01563D

60. Yang L, Xiao Y, Han G, et al (2020) Enhanced stability and efficiency of perovskite solar cells via bifunctional group passivation with thiosalicylic acid. Organic Electronics 81:105681. https://doi.org/10.1016/j.orgel.2020.105681

61. Wang S, Li H, Zhang B, et al (2020) Perovskite solar cells based on the synergy between carbon electrodes and polyethylene glycol additive with excellent stability. Organic Electronics 83:105734. https://doi.org/10.1016/j.orgel.2020.105734

62. Li T, Pan Y, Wang Z, et al (2017) Additive engineering for highly efficient organic–inorganic halide perovskite solar cells: recent advances and perspectives. J Mater Chem A 5:12602–12652. https://doi.org/10.1039/C7TA01798G

63. Koushik D, Verhees WJH, Kuang Y, et al (2017) High-efficiency humidity-stable planar perovskite solar cells based on atomic layer architecture. Energy Environ Sci 10:91–100. https://doi.org/10.1039/C6EE02687G

64. Tan D, Zhang X, Liu X, et al (2020) Stability enhancement of inverted perovskite solar cells using LiF in electron transport layer. Organic Electronics 80:105613. https://doi.org/10.1016/j.orgel.2019.105613

65. Sidhik S, Rosiles Pérez C, Serrano Estrada MA, et al (2020) Improving the stability of perovskite solar cells under harsh environmental conditions. Solar Energy 202:438–445. https://doi.org/10.1016/j.solener.2020.03.034

66. Christians JA, Fung RCM, Kamat PV (2014) An Inorganic Hole Conductor for Organo-Lead Halide Perovskite Solar Cells. Improved Hole Conductivity with Copper Iodide. J Am Chem Soc 136:758–764. https://doi.org/10.1021/ja411014k

67. You J, Meng L, Song T-B, et al (2016) Improved air stability of perovskite solar cells via solution-processed metal oxide transport layers. Nature Nanotechnology 11:75–81. https://doi.org/10.1038/nnano.2015.230

68. Liu Y, Zhang Z, Gao H, et al (2019) A novel inorganic hole-transporting material of CuInS2 for perovskite solar cells with high efficiency and improved stability. Organic Electronics 75:105430. https://doi.org/10.1016/j.orgel.2019.105430

69. Wang K, Olthof S, Subhani WS, et al (2020) Novel inorganic electron transport layers for planar perovskite solar cells: Progress and prospective. Nano Energy 68:104289. https://doi.org/10.1016/j.nanoen.2019.104289

70. Babayigit A, Ethirajan A, Muller M, Conings B (2016) Toxicity of organometal halide perovskite solar cells. Nature Materials 15:247–251. https://doi.org/10.1038/nmat4572

71. Klug MT, Osherov A, Haghighirad AA, et al (2017) Tailoring metal halide perovskites through metal substitution: influence on photovoltaic and material properties. Energy Environ Sci 10:236–246. https://doi.org/10.1039/C6EE03201J

72. Chatterjee S, Pal AJ (2018) Influence of metal substitution on hybrid halide perovskites: towards lead-free perovskite solar cells. J Mater Chem A 6:3793–3823. https://doi.org/10.1039/C7TA09943F

73. Eperon GE, Ginger DS (2017) B-Site Metal Cation Exchange in Halide Perovskites. ACS Energy Lett 2:1190–1196. https://doi.org/10.1021/acsenergylett.7b00290

74. Frolova LA, Anokhin DV, Gerasimov KL, et al (2016) Exploring the Effects of the Pb2+ Substitution in MAPbI3 on the Photovoltaic Performance of the Hybrid Perovskite Solar Cells. J Phys Chem Lett 7:4353–4357. https://doi.org/10.1021/acs.jpclett.6b02122

75. Li M, Wang Z-K, Zhuo M-P, et al (2018) Pb–Sn–Cu Ternary Organometallic Halide Perovskite Solar Cells. Advanced Materials 30:1800258. https://doi.org/10.1002/adma.201800258

76. Shirahata Y, Oku T (2017) Photovoltaic properties of Cu-doped CH3NH3PbI3 with perovskite structure. AIP Conference Proceedings 1807:020008. https://doi.org/10.1063/1.4974790

77. Oku T (2015) Crystal Structures of CH3NH3PbI3 and Related Perovskite Compounds Used for Solar Cells. Solar Cells - New Approaches and Reviews. https://doi.org/10.5772/59284

78. Leguy AMA, Hu Y, Campoy-Quiles M, et al (2015) Reversible Hydration of CH3NH3PbI3 in Films, Single Crystals, and Solar Cells. Chem Mater 27:3397–3407. https://doi.org/10.1021/acs.chemmater.5b00660

79. Barrett CS, Massalski TB (1980) Structure of Metals: Crystallographic Methods, Principles and Data, 3rd revised edition. Pergamon Press Oxford

80. Scherrer P (1918) Bestimmung der Größe und der inneren Struktur von Kolloidteilchen mittels Röntgenstrahlen

81. Langford JI, Wilson AJC (1978) Scherrer after sixty years: A survey and some new results in the determination of crystallite size. Journal of Applied Crystallography. https://doi.org/10.1107/S0021889878012844

82. Uvarov V, Popov I (2013) Metrological characterization of X-ray diffraction methods at different acquisition geometries for determination of crystallite size in nano-scale materials. Materials Characterization 85:111–123. https://doi.org/10.1016/j.matchar.2013.09.002

83. Li Y, Sun W, Yan W, et al (2015) High-Performance Planar Solar Cells Based On CH3NH3PbI3-xClx Perovskites with Determined Chlorine Mole Fraction. Advanced Functional Materials 25:4867–4873. https://doi.org/10.1002/adfm.201501289

84. Tauc J (1974) Amorphous and Liquid Semiconductors. Springer US

85. Singh RK, Kumar A, Jain N, et al (2017) Solution Processed Hybrid Organic-Inorganic CH3NH3PbI3 Perovskite Material and Optical Properties. Materials Today: Proceedings 4:12661–12665. https://doi.org/10.1016/j.matpr.2017.10.079